



# Introducing phosphorus into spinel nickel ferrite to enhance lattice oxygen participation towards water oxidation electrocatalysis

Yuxin Li <sup>a</sup>, Zhe Zhang <sup>a</sup>, Chenguang Li <sup>a</sup>, Yong Zhou <sup>a</sup>, Xiao-Bo Chen <sup>b</sup>, Haiyan Lu <sup>a</sup>, Zhan Shi <sup>a,\*</sup>, Shouhua Feng <sup>a</sup>

<sup>a</sup> State Key Laboratory of Inorganic Synthesis and Preparative Chemistry, College of Chemistry, Jilin University, Changchun 130012, PR China

<sup>b</sup> School of Engineering, RMIT University, Carlton, VIC 3053, Australia



## ARTICLE INFO

**Keywords:**  
Phosphorus introduction  
Nickel ferrite  
Lattice oxygen oxidation mechanism  
O 2p band center  
DFT calculation

## ABSTRACT

Oxygen evolution reaction (OER) restricts the efficiency of overall water splitting due to its complex transfer process and sluggish intrinsic kinetics. The novel lattice oxygen oxidation mechanism (LOM) could lift the theoretical scaling limits of the traditional adsorbate evolution mechanism (AEM), but increasing the participation of lattice oxygen still remains a great challenge. Herein, we introduce phosphorus into spinel nickel ferrite as electrocatalyst with an overpotential of 264 mV at 10 mA cm<sup>-2</sup> towards water oxidation. Experimental results confirm the enhanced participation of lattice oxygen for OER in P-NiFe<sub>2</sub>O<sub>4</sub>. Further theoretical modelling reveals that the incorporated phosphorus results in an upshift of O 2p band center relative to Fermi level and enhances hybridization of the metal-oxygen bond, thus facilitating LOM and accelerating the OER process on spinel NiFe<sub>2</sub>O<sub>4</sub>. This work provides some deep insights into the OER mechanism and a sound strategy for improving the electrocatalytic activity of spinel oxides.

## 1. Introduction

Hydrogen (H<sub>2</sub>) has emerged as one of the most promising substitutes to traditional fossil fuels due to its clean nature and high energy density [1,2]. Electrocatalytic water splitting (EWS) which employs electricity represents an ideal option for carbon-free hydrogen production, but the overall efficiency is intrinsically limited by the anodic oxygen evolution reaction (OER) with a complex four-electron transfer process to a great extent [3,4]. To date, precious metal-based catalysts (RuO<sub>2</sub>, IrO<sub>2</sub>, etc.) still hold the benchmarking activity for electrocatalytic OER, but they are stagnant in wide application on account of the resource scarcity, low selectivity and high cost [5,6]. Accordingly, it is indispensable to construct and develop stable and noble-metal-free electrocatalysts with superior performance for OER.

To develop efficient OER catalysts with desirable performance, fundamental understandings of OER mechanism is of paramount significance. In terms of the traditional adsorbate evolution mechanism (AEM) with four concerted proton-electron transfer (CPET) reactions, the oxygen precursors experience a step-by-step “adsorption-deprotonation-coupling-desorption” process (namely, \*OH → \*O → \*OOH → O<sub>2</sub>) [7–9]. The binding energy of the oxygen-containing intermediates could

be optimized via engineering the electronic structure. However, a universal scaling relation between the binding energies of \*OOH and \*OH is fitted to be  $\Delta G_{*OOH} = \Delta G_{*OH} + 3.2$  (eV) based upon DFT calculations, which indicates an overpotential of at least 370 mV in AEM theoretically [10–12]. Based on the scaling limitation, the avoidance of \*OOH intermediate production during OER process would be helpful to bypass the intrinsic obstacle of AEM [13]. Recently, a novel lattice oxygen-mediated mechanism (LOM) has been proposed in some solid-state metal oxide/(oxy)hydroxide electrocatalysts, enabling the lattice oxygen to participate in the formation of oxygen molecules [14–16]. In the LOM pathway, direct O-O formation could be achieved by the coupling between the \*O intermediate and lattice oxygen, which enables breakthrough in the thermodynamic limitations of AEM [17, 18]. Thus, it is essential to understand how to regulate the lattice oxygen activity and facilitate the efficient LOM route.

Generally, the metal *d*-band center theory could offer valuable guidance to the construction of catalyst based on AEM, similarly, the oxygen *p*-band center theory could also play as an alternative descriptor for OER [19–22]. The covalency of the M-O interaction could be reflected by the O *p*-band relative to the Fermi level (*E*<sub>F</sub>), directly influencing the electron transfer. According to previously reported studies, a

\* Corresponding author.

E-mail address: [zshi@mail.jlu.edu.cn](mailto:zshi@mail.jlu.edu.cn) (Z. Shi).

number of strategies have been applied to trigger the LOM pathway, such as increasing concentration of the oxygen vacancy [23], enlarging the M–O bond polarizability [24], designing high-valence oxides (HVOs) to promote the charge transfer between the metal *d* band and oxygen *p* band [22,25], decorating the surface with single atoms to induce an upshift of the oxygen *p* band and increase orbital overlap, therefore achieving a stronger covalency of the M–O interactions [26].

Of various transition metal (TM) oxides/(oxy)hydroxides, spinel-type oxides ( $AB_2O_4$ ) have been investigated extensively and exhibited desirable and outstanding performance towards water oxidation reaction due to their low cost and high stability [27,28]. In a typical  $AB_2O_4$  crystal structure, metal cations ( $A^{2+}$  and  $B^{3+}$ ) are filled into tetrahedral ( $TM_{td}$ ) and octahedral ( $TM_{oct}$ ) interstices respectively, and the oxygen anions are arranged in a cubic-packed lattice [29]. According to the distribution of metallic ions in the tetrahedral and octahedral sites, spinel-structured oxides could be categorized into normal spinels, inverse spinels and complex spinels [30]. In particular, for inverse spinels, half  $B^{3+}$  cations occupy the tetrahedral sites, while the octahedral sites are occupied by all  $A^{2+}$  cations and another half  $B^{3+}$  cations [25]. Generally, in spinel oxide lattice, the oxygen anion is shared by  $TM_{td}$  cations and  $TM_{oct}$  cations, which could influence the orbital overlap between metal and oxygen, thus suffering from weak covalency and preferring AEM pathway to proceed OER process [31]. It has been reported that the introduction of heteroatom could modulate the electronic structures and distributions, further optimizing the position of band center to achieve high electrocatalytic performance and stability [12,32,33].

Inspired by above consideration, we aimed to enhance the lattice oxygen participation by the introduction of phosphorus atom into the spinel nickel ferrite ( $NiFe_2O_4$ ) nanosheets. The prepared P- $NiFe_2O_4$  catalyst demonstrates an overpotential of 264 mV at the current density of  $10 \text{ mA cm}^{-2}$ , which was  $\approx 90$  mV lower than that of pristine  $NiFe_2O_4$  nanosheets in 1.0 M KOH. Combination of electrochemical measurements and density functional theory (DFT) calculations confirms that the phosphorus incorporation could reduce the energy barrier and upshift the O 2*p* band center relative to Fermi level ( $E_F$ ), which was key to the enhancement of lattice participation on spinel  $NiFe_2O_4$ . The LOM mechanism plays a dominant role in P- $NiFe_2O_4$  composite, thus possessing an accelerated OER kinetics than pristine  $NiFe_2O_4$ . This work could pave a pathway to activate lattice oxygen and benefit LOM on oxygen-inert spinel composites, further achieving boosted and outstanding performance towards water oxidation reaction.

## 2. Experimental section

### 2.1. Preparation of $NiFe(OH)_x$

0.5 g ferric nitrate nonahydrate ( $Fe(NO_3)_3 \cdot 9 H_2O$ ), 0.5 g nickel nitrate hexahydrate ( $Ni(NO_3)_2 \cdot 6 H_2O$ ), 0.3 g  $NH_4F$  and 1.2 g urea were first dissolved in 40 mL deionized water under continuous stirring at room temperature. Then the obtained solution was transferred into a Teflon-lined stainless-steel autoclave and maintained at 100 °C for 16 h. After it cooled to room temperature, the powder was collected via centrifugation at an rpm of 8000 and washed with water and ethanol several times, and then dried at 80 °C.

### 2.2. Preparation of $NiFe_2O_4$ and P- $NiFe_2O_4$

Typically,  $NiFe(OH)_x$  powder was annealed at 500 °C for 2 h with a heating rate of 5 °C/min. Then the as-prepared sample (20 mg) was placed downstream in a tube furnace with different amount of  $NaH_2PO_2$  (10, 30, 50 and 70 mg) in the upstream, and the *in-situ* phosphorization reaction was carried out at different temperatures (300 °C, 350 °C, 400 °C and 450 °C) with a heating speed of 3 °C/min for 2 h. The final product was collected after cooling down and denoted as P- $NiFe_2O_4$ . The optimal synthetic condition was 30 mg  $NaH_2PO_2$  under 400 °C in this

work.

### 2.3. Material characterizations

Powder X-ray diffraction (XRD) patterns of the synthesized composites were conducted on Rigaku D/MAX-2550/PC with Cu  $K\alpha$  radiation in the range from 20° to 80°. The accelerating voltage and applied current were 40 kV and 120 mA, respectively. To observe the morphology of the samples, scanning electron microscopy (SEM) images were collected with the operating voltage of 3 kV on a JEOL JSM-7800 F. Transition electron microscopy (TEM) images and high-resolution TEM (HR-TEM) images were obtained with a Talos F200S microscope equipped with a field emission gun operating at 200 kV. The surface electronic states and chemical composition of the as-prepared samples were characterized by X-ray photoelectron spectroscopy (XPS) using Thermo ESCALAB 250. The measured binding energies were calibrated based on the C 1 s binding energy at 284.8 eV. Nitrogen adsorption-desorption analysis was conducted on ASAP 2020 (Micromeritics instrument, USA) after degassing at 120 °C for 12 h. Raman tests were conducted using an inVia (Renishaw Company) instrument with irradiation at 532 nm.

### 2.4. Electrochemical measurements

Electrochemical measurements were performed on a CHI-760E electrochemical working station (Chenhua Corp., Shanghai, China.) in a three-electrode cell at room temperature (25 °C) in 1.0 M KOH. Typically, graphite rod and  $Hg/HgO$  were used as the counter electrode (CE) and reference electrode (RE), respectively. The reversible hydrogen electrode (RHE) converted from  $Hg/HgO$  was obtained from the Nernst equation:  $E(\text{RHE}) = E(Hg/HgO) + 0.059 \text{ pH} + 0.098$ . Before the linear sweep voltammetry (LSV) test, the electrochemical activation of CV was performed at a scan rate of  $100 \text{ mV s}^{-1}$  until the electrodes were stable. The scan rate for the LSV tests was  $5 \text{ mV s}^{-1}$  with 95%  $iR$ -compensated automatically in the potential range of 1.2–1.7 V (vs. RHE). The Tafel slope was obtained from the Tafel equation:  $\eta = a \times \log|j| + b$ , where  $\eta$  is the overpotential,  $j$  is the current density and  $a$  is the Tafel slope. The CV tests with different scan rates (40–140  $\text{mV s}^{-1}$ ) were conducted over non-faradaic potential window. The electrochemically active surface area (ECSA) of the catalyst was calculated from the double-layer capacitance ( $C_{dl}$ ) according to the equation:  $\text{ECSA} = C_{dl}/C_s$ . In our work,  $C_s$  was estimated to be  $40 \mu\text{F cm}^{-2}$  [34]. Chronopotentiometry (CP) and CV measurements were performed to evaluate the stability and durability of the electrocatalyst. The electrochemical impedance spectroscopy (EIS) analysis was performed at 0.6 V (vs.  $Hg/HgO$ ) with an amplitude of 5 mV in the frequency range of 0.01 Hz–100 kHz. The TOF value was calculated through the following formula:  $\text{TOF} = j \cdot S / \alpha \cdot F \cdot n$ , where  $j$  is the current density at 1.53 V (vs. RHE),  $S$  is the surface area of the electrode,  $\alpha$  represents the number of electrons (4 for oxygen evolution reaction),  $F$  is the Faraday constant ( $96485 \text{ C mol}^{-1}$ ) and  $n$  represents the moles of active sites of the tested samples.

To explore the dominant mechanism of  $NiFe_2O_4$  and P- $NiFe_2O_4$  during the OER process, we conducted electrochemical tests at different concentrations of KOH electrolyte with the pH from 12 to 14, respectively. Furthermore, LSV measurement was also conducted in 1.0 M KOH and 1.0 M TMAOH solutions, respectively.

Chemicals and reagents, electrode preparation and computation methods are specifically described in [Supporting Information](#).

## 3. Results and discussion

### 3.1. Synthesis and characterizations of the catalyst

P- $NiFe_2O_4$  was prepared via a simple three-step approach, as schematically illustrated in [Fig. 1A](#). Initially,  $NiFe(OH)_x$  composite was fabricated through a straightforward hydrothermal strategy with an

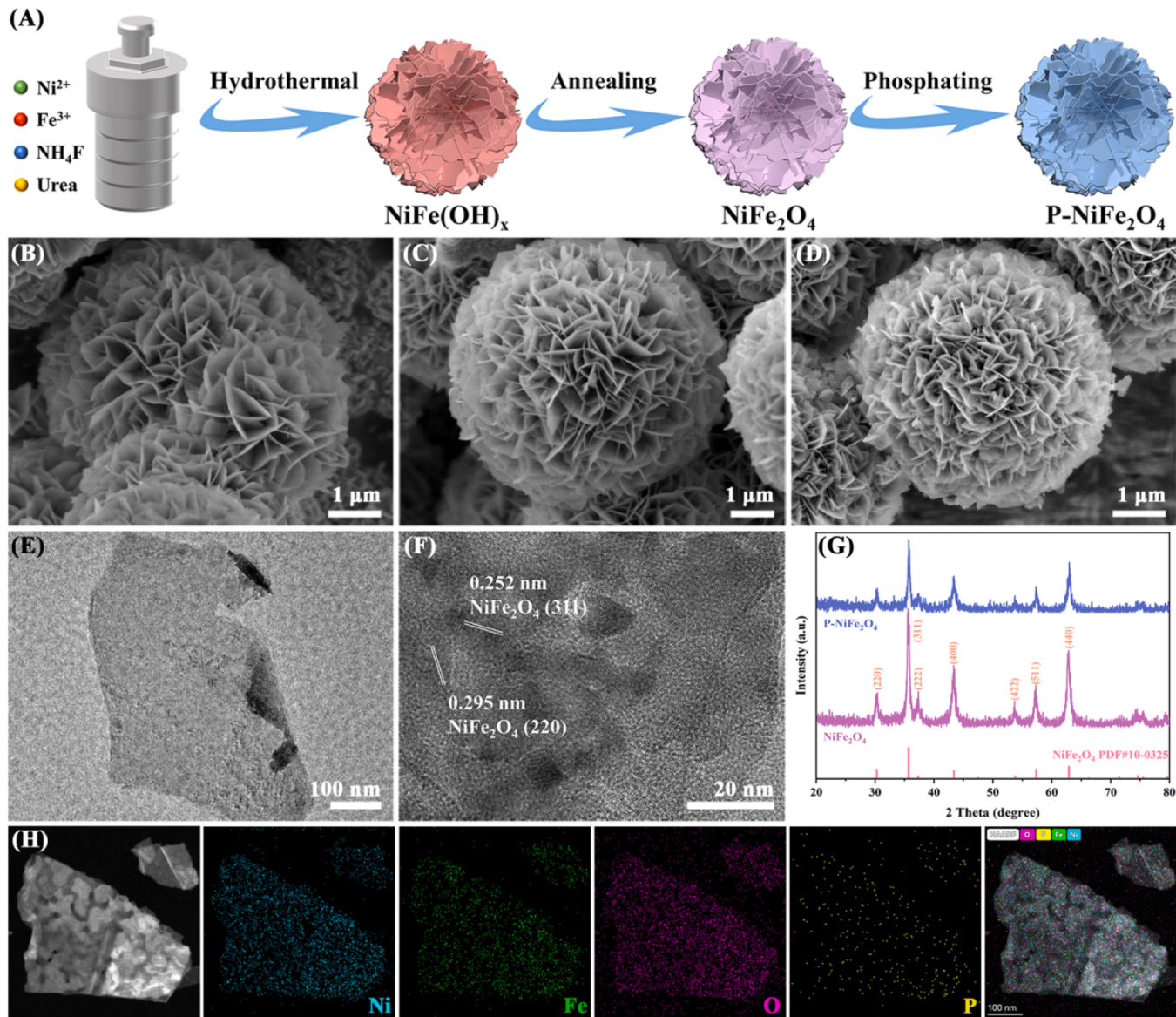


**Fig. 1.** (A) Schematic illustration of the formation process of  $\text{P-NiFe}_2\text{O}_4$ . SEM images of (B)  $\text{NiFe(OH)}_x$ , (C)  $\text{NiFe}_2\text{O}_4$  and (D)  $\text{P-NiFe}_2\text{O}_4$ . (E) TEM image of  $\text{P-NiFe}_2\text{O}_4$ . (F) HR-TEM image of  $\text{P-NiFe}_2\text{O}_4$ . (G) XRD patterns of  $\text{NiFe}_2\text{O}_4$  and  $\text{P-NiFe}_2\text{O}_4$ . (H) HAADF-STEM image and corresponding elemental mapping images of  $\text{P-NiFe}_2\text{O}_4$ .

aqueous solution of nickel nitrate, ferric nitrate, urea and ammonium fluoride. Subsequently,  $\text{NiFe}_2\text{O}_4$  was synthesized by annealing the as-prepared  $\text{NiFe(OH)}_x$  powder, and phosphorus incorporation into  $\text{NiFe}_2\text{O}_4$  (denoted as  $\text{P-NiFe}_2\text{O}_4$ ) was achieved after *in-situ* low-temperature phosphating, in the presence of sodium hypophosphite ( $\text{NaH}_2\text{PO}_2$ ) as phosphorus source to produce phosphine ( $\text{PH}_3$ ) gas [35, 36]. Scanning electron microscopy (SEM) was conducted to characterize the surface morphology of the as-prepared samples. SEM images (Fig. 1B-C, Fig. S1) reveal that both  $\text{NiFe(OH)}_x$  and  $\text{NiFe}_2\text{O}_4$  featured a typical two-dimensional nanosheet structure, and the morphology remained after the incorporation of phosphorus into  $\text{NiFe}_2\text{O}_4$  during the phosphating process (Fig. 1D). Corresponding transmission electron microscopy (TEM) image also confirmed the nanosheet morphology of  $\text{NiFe}_2\text{O}_4$  and  $\text{P-NiFe}_2\text{O}_4$  (Fig. 1E, Fig. S2). Furthermore, the interface structure was investigated through high-resolution TEM (HR-TEM). The as-observed clear lattice fringes with the interplanar spacings of 0.252 nm and 0.295 nm were in agreement with the (311) and (220) planes of spinel  $\text{NiFe}_2\text{O}_4$ , respectively (Fig. 1F, Fig. S3) [37].

X-ray powder diffraction (XRD) measurement was conducted to shed light on the crystalline structure and composition of the synthesized

samples. The XRD patterns of  $\text{NiFe}_2\text{O}_4$  and  $\text{P-NiFe}_2\text{O}_4$  all matched with the cubic  $\text{NiFe}_2\text{O}_4$  phase (JCPDS Card No. 10-0325) with no other impurities (Fig. 1G) [25,38]. The diffraction peaks located at 30.4°, 35.6°, 37.3°, 43.3°, 53.7°, 57.3° and 62.8° were ascribed to the (220), (311), (222), (400), (422), (511) and (440) facets of  $\text{NiFe}_2\text{O}_4$ , respectively [4, 28]. It could be noticed that there was no additional peak related to metal phosphide (like  $\text{NiP}_x$  or  $\text{FeP}_x$ ) due to the small quantity of phosphorus source and the low reaction temperature. Inductively coupled plasma-optical emission spectrometer (ICP-OES) measurement demonstrated that the content of phosphorus in  $\text{P-NiFe}_2\text{O}_4$  nanosheet was calculated to be about 1.76 wt%, which was close to the EDS result (Table. S1, Fig. S4). Furthermore, high-angle annular dark-field scanning transmission electron microscopy (HAADF-STEM, Fig. 1H) revealed that the elements of Ni, Fe, O and P were distributed homogeneously throughout the nanosheet, indicating the successful introduction of phosphorus into  $\text{NiFe}_2\text{O}_4$ .

Raman spectroscopy was performed to determine the chemical environment and electronic structure of the as-synthesized catalysts, as presented in Fig. 2A [39]. The Raman spectra of  $\text{NiFe}_2\text{O}_4$  and  $\text{P-NiFe}_2\text{O}_4$  both exhibited five typical Raman active modes ( $3\text{ F}_{2g} + \text{E}_g + \text{A}_{1g}$ ),

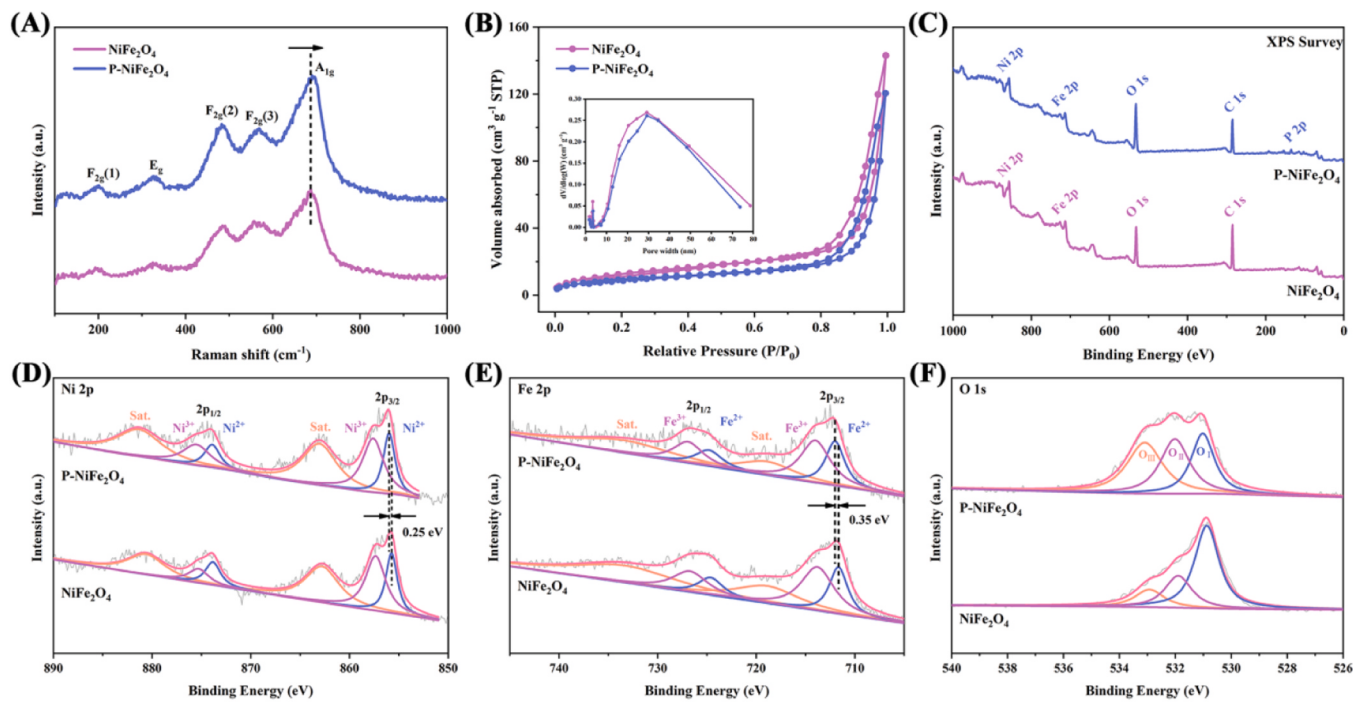


**Fig. 2.** (A) Raman spectra of NiFe<sub>2</sub>O<sub>4</sub> and P-NiFe<sub>2</sub>O<sub>4</sub>. (B) N<sub>2</sub> adsorption-desorption isotherms of NiFe<sub>2</sub>O<sub>4</sub> and P-NiFe<sub>2</sub>O<sub>4</sub>. Inset: the pore size distribution of NiFe<sub>2</sub>O<sub>4</sub> and P-NiFe<sub>2</sub>O<sub>4</sub>. (C) XPS full survey patterns of NiFe<sub>2</sub>O<sub>4</sub> and P-NiFe<sub>2</sub>O<sub>4</sub>. High-resolution (D) Ni 2p, (E) Fe 2p and (F) O 1s spectra of NiFe<sub>2</sub>O<sub>4</sub> and P-NiFe<sub>2</sub>O<sub>4</sub>.

which was consistent with the crystal structure with *Fd-3m* space group [40,41]. No other peaks belonging to Ni or Fe phosphides were detected, which was in agreement with the XRD measurement results. It also proved that the crystal structure of NiFe<sub>2</sub>O<sub>4</sub> was not destroyed by the low-temperature phosphating procedure. Specifically, the E<sub>g</sub> mode at Raman shift of 324 cm<sup>-1</sup> and A<sub>1g</sub> mode at 690 cm<sup>-1</sup> were assigned to the vibration of sub-lattices at tetrahedral and octahedral sites, respectively. As for three F<sub>2g</sub> modes, F<sub>2g</sub>(1) at ~200 cm<sup>-1</sup> demonstrated the symmetric bending and stretching of M-O bond with tetrahedral coordination environment, while F<sub>2g</sub>(2) and F<sub>2g</sub>(3) at 490 cm<sup>-1</sup> and 570 cm<sup>-1</sup> were based on the asymmetric stretching and bending modes of M-O bond in octahedron [28]. It could be seen that the position of A<sub>1g</sub> mode for P-NiFe<sub>2</sub>O<sub>4</sub> exhibited a blue shift compared with NiFe<sub>2</sub>O<sub>4</sub>, indicating the modified electronic properties after phosphorization [42]. Specific Brunauer-Emmett-Teller (BET) surface areas of NiFe<sub>2</sub>O<sub>4</sub> and P-NiFe<sub>2</sub>O<sub>4</sub> nanosheets were measured to be 46.96 and 33.02 m<sup>2</sup> g<sup>-1</sup>, respectively. The collapse of some pores during the phosphating process might result in the decrease in the surface area. It can be seen that the nitrogen adsorption-desorption isotherms of NiFe<sub>2</sub>O<sub>4</sub> and P-NiFe<sub>2</sub>O<sub>4</sub> exhibited a typical type-II isotherm with an evident hysteresis loop, suggesting the existence of mesoporous structures in these two samples (Fig. 2B) [43]. In addition, we employed the most commonly used Barrett-Joyner-Halenda (BJH) model to calculate the pore size distributions of NiFe<sub>2</sub>O<sub>4</sub> and P-NiFe<sub>2</sub>O<sub>4</sub>. The result inset of Fig. 2B shows that the porous NiFe<sub>2</sub>O<sub>4</sub> and P-NiFe<sub>2</sub>O<sub>4</sub> nanosheets had mesopore peak mainly in a range of 20–50 nm, and such mesoporous structure could facilitate to expose more active sites, thus promoting the whole electrocatalytic process [27,44].

In order to determine the surface compositions and electronic properties of the electrocatalysts, X-ray photoelectron spectroscopy (XPS) was further conducted. As depicted in Fig. 2C, the XPS survey of P-NiFe<sub>2</sub>O<sub>4</sub> demonstrated the presence of Ni, Fe, O and P elements with no impurities, consistent with the above elemental mapping results. The high-resolution Ni 2p spectrum of P-NiFe<sub>2</sub>O<sub>4</sub> could be distinguished into two satellite peaks and four spin-orbit doublets, implying the co-existence of Ni<sup>2+</sup> and Ni<sup>3+</sup> states in P-NiFe<sub>2</sub>O<sub>4</sub> (Fig. 2D). The peaks centered at 855.98 eV (2p<sub>3/2</sub>) and 873.9 eV (2p<sub>1/2</sub>) were assigned to

Ni<sup>2+</sup>, whereas the peaks at 857.6 eV (2p<sub>3/2</sub>) and 875.5 eV (2p<sub>1/2</sub>) belonged to Ni<sup>3+</sup>, accompanied by two satellite peaks (Sat.) at 863.04 eV and 881.26 eV. Notably, compared with NiFe<sub>2</sub>O<sub>4</sub>, the Ni 2p for P-NiFe<sub>2</sub>O<sub>4</sub> was blue-shifted for approximately 0.25 eV and the peak area ratio of Ni<sup>3+</sup>/Ni<sup>2+</sup> increased from 1.57 to 1.65, indicating that the introduction of phosphorus into NiFe<sub>2</sub>O<sub>4</sub> could result in the decrease in the electron density around Ni species and an increased valence state of Ni (Table. S2) [45]. In addition, regarding the high-resolution Fe 2p spectrum of P-NiFe<sub>2</sub>O<sub>4</sub>, the fitted peaks of Fe 2p<sub>3/2</sub> and Fe 2p<sub>1/2</sub> at around 712 eV and 724.8 eV were attributed to Fe<sup>2+</sup>, and the two orbits of Fe<sup>3+</sup> centered at 713.99 eV (2p<sub>3/2</sub>) and 726.91 eV (2p<sub>1/2</sub>), respectively (Fig. 2E). Moreover, two broad peaks located at 718.87 eV and 733.33 eV were the typical satellite peaks (Sat.) of Fe 2p<sub>3/2</sub> and Fe 2p<sub>1/2</sub> [46]. It could be noticed that the binding energy of Fe 2p<sub>3/2</sub> moved positively (+ 0.35 eV) and the peak area ratio of Fe<sup>3+</sup>/Fe<sup>2+</sup> was 1.63, higher than that of NiFe<sub>2</sub>O<sub>4</sub> (1.47) (Table. S3). Similarly, the phosphorization of NiFe<sub>2</sub>O<sub>4</sub> also increased the valence of the Fe species. According to previous works, increasing the metal valence will enhance the orbital hybridization between the metal 3d and O 2p orbitals, resulting in a strengthened M-O covalent bond that favors the LOM mechanism [10,26]. When turning to the O 1s spectra of NiFe<sub>2</sub>O<sub>4</sub> and P-NiFe<sub>2</sub>O<sub>4</sub>, they could be deconvoluted into three peaks denoted as O<sub>I</sub>, O<sub>II</sub>, and O<sub>III</sub> (Fig. 2F). To be specific, the O<sub>I</sub> peak with the binding energy of 530.5 eV was attributed to the lattice oxygen (M-O) in metal oxides, whereas O<sub>II</sub> centered at 531.8 eV could be described as the oxygen vacancy (O<sub>V</sub>) [45, 47]. After the introduction of phosphorus, the peak area percentage of O<sub>V</sub> increased from 25.32% in NiFe<sub>2</sub>O<sub>4</sub> to 33.22% for P-NiFe<sub>2</sub>O<sub>4</sub> (Table. S4). It has been reported that a high concentration of oxygen vacancies could also benefit the LOM pathway [22]. Additionally, the peak of O<sub>III</sub> at ~533 eV corresponded to the water molecules absorbed on the surface [48,49]. The P 2p spectrum of P-NiFe<sub>2</sub>O<sub>4</sub> was displayed in Fig. S5, the peaks at ~134 eV and 129.8 eV could be assigned to the phosphate exposed to air (P-O) and metal-phosphorus bond (M-P) [50].

### 3.2. Electrocatalytic performance for OER in alkaline media

The electrocatalytic oxygen evolution properties of the synthesized

samples were evaluated using a standard three-electrode cell in 1.0 M KOH solution. Commercial RuO<sub>2</sub> was also tested for comparison. Initially, in order to explore the effects of the phosphating temperature and quantity of NaH<sub>2</sub>PO<sub>4</sub> on the electrocatalytic activity, the OER performances of P-NiFe<sub>2</sub>O<sub>4</sub> prepared with different amount of NaH<sub>2</sub>PO<sub>4</sub> (10, 30, 50 and 70 mg) under different temperatures (300, 350, 400 and 450 °C) were tested (Fig. S6-8). The testing results suggested that the optimal synthetic condition was 30 mg NaH<sub>2</sub>PO<sub>4</sub> under 400 °C. Thus, the typical sample of P-NiFe<sub>2</sub>O<sub>4</sub> (30 mg, 400 °C) was selected to be primarily studied due to its optimized electrocatalytic activity. Fig. 3A and Fig. S9 display the linear sweep voltammetry (LSV) curves of the prepared samples. As seen, P-NiFe<sub>2</sub>O<sub>4</sub> showed favorable OER electrocatalytic performance, requiring an overpotential of 264 mV to reach the current density of 10 mA cm<sup>-2</sup>, lower than that of NiFe(OH)<sub>x</sub> (363 mV), NiFe<sub>2</sub>O<sub>4</sub> (355 mV) and commercial RuO<sub>2</sub> (290 mV). The overpotentials to achieve the current densities of 10 mA cm<sup>-2</sup>, 50 mA cm<sup>-2</sup> and 100 mA cm<sup>-2</sup> in OER were displayed in Fig. 3B, suggesting that P-NiFe<sub>2</sub>O<sub>4</sub> also had more desirable performance than other electrocatalysts even at relatively higher current densities. To gain

insight into the OER kinetics, the linear region of LSV curve was investigated by Tafel plot (Fig. 3C). The derived Tafel slopes were fitted to be 110.44, 75.13, 87.05 and 43.30 mV dec<sup>-1</sup> for NiFe(OH)<sub>x</sub>, NiFe<sub>2</sub>O<sub>4</sub>, RuO<sub>2</sub> and P-NiFe<sub>2</sub>O<sub>4</sub>, respectively, suggesting the accelerated OER kinetics for P-NiFe<sub>2</sub>O<sub>4</sub>. Fig. 3D and Table S5 show a comparison of the recently reported overpotentials and Tafel slopes of the relevant spinel-based electrocatalysts. The OER properties of P-NiFe<sub>2</sub>O<sub>4</sub> electrocatalyst prepared in this work is also competitive to those spinel-based composites. Electrochemical impedance spectroscopy (EIS) was then measured to study the interfacial reactions and behavior of the as-prepared catalysts (Fig. 3E). After fitting the EIS curves by using a simplified equivalent circuit, the semicircle diameters apparently decreased in the order of NiFe(OH)<sub>x</sub> (35.9 Ω) > NiFe<sub>2</sub>O<sub>4</sub> (21.2 Ω) > RuO<sub>2</sub> (8.67 Ω) > P-NiFe<sub>2</sub>O<sub>4</sub> (5.61 Ω), revealing that the P-NiFe<sub>2</sub>O<sub>4</sub> had the lowest charge transfer resistance ( $R_{ct}$ ) across the electrode/electrolyte interface and improved electrical conductivity (Fig. S10, Table S6). This trend was also compatible with the polarization results and Tafel slopes.

In order to clarify the possible origins of such catalytic performance,

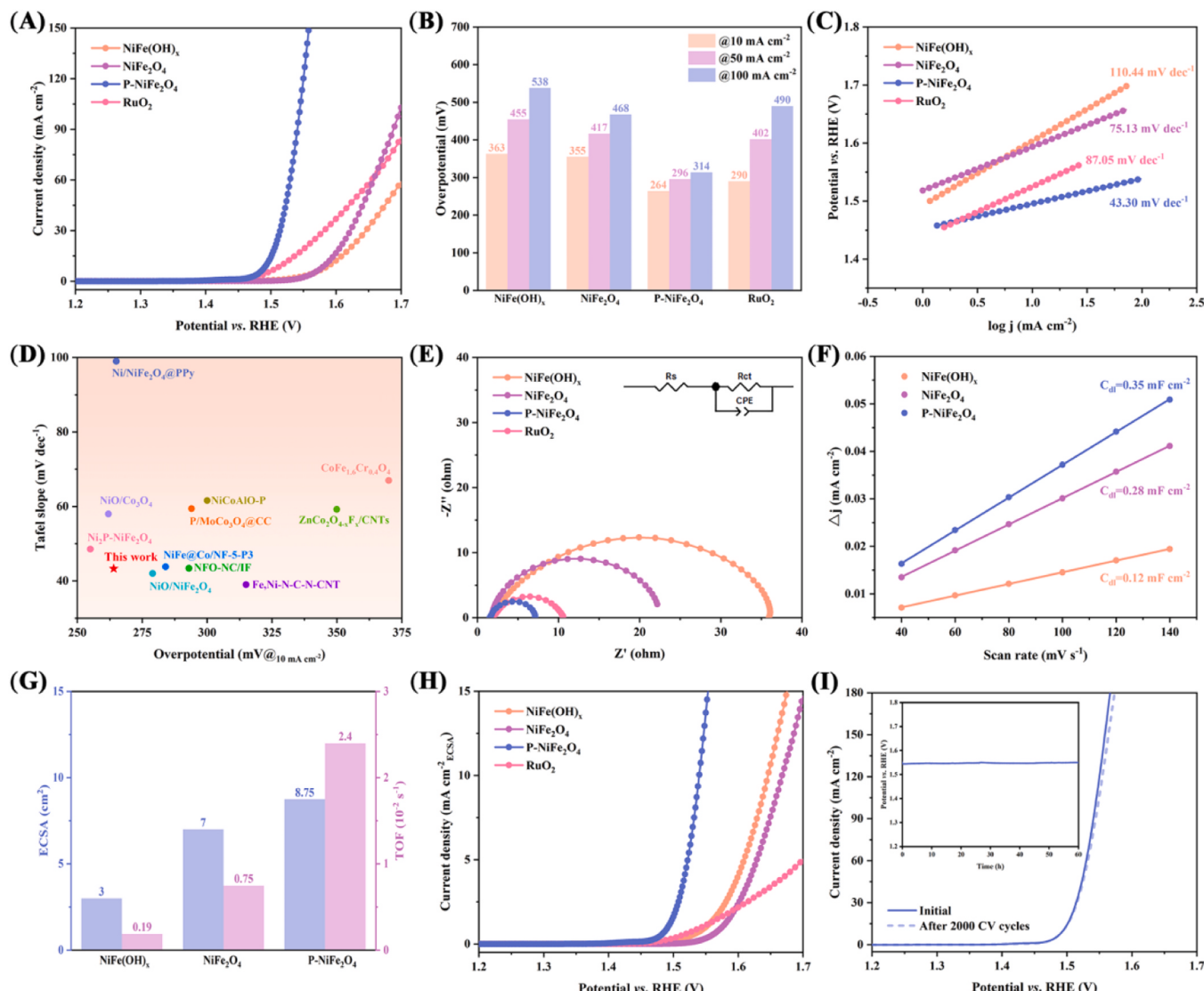


**Fig. 3.** Electrochemical performances of the as-prepared electrocatalysts in 1.0 M KOH. (A) Polarization curves. (B) The overpotentials to achieve the current densities of 10, 50 and 100 mA cm<sup>-2</sup>. (C) Tafel plots. (D) Overpotentials at 10 mA cm<sup>-2</sup> and Tafel slopes of some spinel-based electrocatalysts reported recently. (E) Nyquist plots of the as-prepared samples. The inset is an equivalent circuit. (F) The fitted  $C_{dl}$  at the non-faradaic potential range. (G) ECSA and TOF (at  $\eta = 300$  mV) of NiFe(OH)<sub>x</sub>, NiFe<sub>2</sub>O<sub>4</sub> and P-NiFe<sub>2</sub>O<sub>4</sub>; (H) Polarization curves with the current density normalized by ECSA. (I) LSV curves for P-NiFe<sub>2</sub>O<sub>4</sub> before and after 2000 CV cycles. Inset: chronopotentiometric durability test for 60 h at 50 mA cm<sup>-2</sup>.

cyclic voltammetry (CV) measurement at different scan rates in the region without redox processes was then carried out to determine the double-layer capacitance ( $C_{dl}$ ), which is proportional to the electrochemically active surface area (ECSA) (Fig. S11). As shown in Fig. 3F, P-NiFe<sub>2</sub>O<sub>4</sub> exhibited the  $C_{dl}$  value of 0.35 mF cm<sup>-2</sup> and the ECSA values were calculated to be 3 cm<sup>2</sup>, 7 cm<sup>2</sup>, 8.75 cm<sup>2</sup> and 17 cm<sup>2</sup> for NiFe(OH)<sub>x</sub>, NiFe<sub>2</sub>O<sub>4</sub>, P-NiFe<sub>2</sub>O<sub>4</sub>, and commercial RuO<sub>2</sub>, respectively (Fig. 3G). Accordingly, we further normalized the polarization curves of different electrocatalysts by ECSA, demonstrating that the intrinsic OER catalytic activity ranked in the order: P-NiFe<sub>2</sub>O<sub>4</sub> > NiFe(OH)<sub>x</sub> > NiFe<sub>2</sub>O<sub>4</sub> > RuO<sub>2</sub> (Fig. 3H). For P-NiFe<sub>2</sub>O<sub>4</sub>, it achieved the current density of ~34.25 mA cm<sup>-2</sup> at 1.6 V (vs. RHE), which was 8.46 times of NiFe(OH)<sub>x</sub>, 14.45 times of NiFe<sub>2</sub>O<sub>4</sub> and 15.8 times of RuO<sub>2</sub>. This result also implied that although the ECSA of P-NiFe<sub>2</sub>O<sub>4</sub> was smaller than that of commercial RuO<sub>2</sub>, it still had the highest intrinsic OER performance among the four tested samples. Besides, the MA (mass activity) and SA (area ratio activity) were also calculated and the results also proved the superior OER catalytic performance of P-NiFe<sub>2</sub>O<sub>4</sub> (Fig. S12). Meanwhile, turnover frequency (TOF) was further investigated to fully understand the intrinsic catalytic activity of the developed electrodes. In this work, we assumed that all the Ni and Fe atoms on the surface were possible catalytically active sites in the calculations. At the overpotential of 300 mV, the calculated TOF value of P-NiFe<sub>2</sub>O<sub>4</sub> was 0.024 s<sup>-1</sup>, which was significantly greater than that of NiFe(OH)<sub>x</sub> (0.0019 s<sup>-1</sup>) and NiFe<sub>2</sub>O<sub>4</sub> (0.0075 s<sup>-1</sup>), indicating that the incorporated phosphorus into NiFe<sub>2</sub>O<sub>4</sub> could contribute largely to the catalytic efficiency (Fig. 3G). Finally, stability is another fundamental descriptor to evaluate the performance of P-NiFe<sub>2</sub>O<sub>4</sub> electrocatalyst in practical applications, which was investigated by the cyclic voltammetry (CV) and chronopotentiometry (CP) methods in this study. As displayed in Fig. 3I, the polarization curves of P-NiFe<sub>2</sub>O<sub>4</sub> before and after 2000 CV cycles almost overlapped, and the overpotential increased approximately 5 mV at 100 mA cm<sup>-2</sup>. In addition, the chronopotentiometric curve for P-NiFe<sub>2</sub>O<sub>4</sub> exhibited an outstanding durability and no obvious increase for the potential at 50 mA cm<sup>-2</sup> can be observed after 60-hour

measurement (inset of Fig. 3I). Compared with commercial RuO<sub>2</sub>, the as-prepared P-NiFe<sub>2</sub>O<sub>4</sub> electrocatalyst not only displayed desirable electrochemical performance towards OER, but also exhibited an outstanding stability (Fig. S13).

### 3.3. Investigations on changes during the reaction

To determine the behaviors and changes of the catalyst during the electrocatalytic reaction, a series of measurements on the post-OER P-NiFe<sub>2</sub>O<sub>4</sub> sample were performed. First, XRD measurement was conducted to investigate the crystalline structural change of P-NiFe<sub>2</sub>O<sub>4</sub> after the long time stability test. It could be seen that the diffraction peaks were well corresponding to NiFe<sub>2</sub>O<sub>4</sub> and no additional peaks (apart from the peaks originating from carbon paper) could be detected in the XRD pattern (Fig. 4A). Subsequently, SEM and TEM measurements were employed to characterize the morphology of the catalyst after the OER test. SEM (Fig. 4B) and TEM images (Fig. S14) detailed the two-dimensional nanosheet structure of P-NiFe<sub>2</sub>O<sub>4</sub>, also confirming the superior structural stability after the measurement. Additionally, the lattice fringes could also be distinguished clearly in the HR-TEM image of the post-OER P-NiFe<sub>2</sub>O<sub>4</sub> (Fig. 4C, Fig. S15). The lattices with the interplanar spacings of 0.241 nm, 0.252 nm and 0.295 nm matched well with the (222), (311) and (220) facets of cubic NiFe<sub>2</sub>O<sub>4</sub>, which was also in good agreement with the above XRD result [51–54]. Energy dispersive spectroscopy (EDS) mapping results also indicated that the Ni, Fe, O and P elements were all preserved and distributed evenly across the catalyst after the long-time stability test on P-NiFe<sub>2</sub>O<sub>4</sub> (Fig. S16).

XPS measurement was then performed in order to investigate the surface chemical state and composition after the catalytic reaction. From the XPS full survey spectra in Fig. 4D, the elements of Ni, Fe, O and P could still be detected, which was also in accord with the elemental mapping results of post-OER P-NiFe<sub>2</sub>O<sub>4</sub>. As for the high-resolution Ni 2p spectrum, it was worth mentioning that the peak area ratio of Ni<sup>3+</sup>/Ni<sup>2+</sup> had a dramatic increase from 1.65 in P-NiFe<sub>2</sub>O<sub>4</sub> to 1.92 after the OER test, indicating the oxidation of Ni species (Fig. 4E). When turning to the

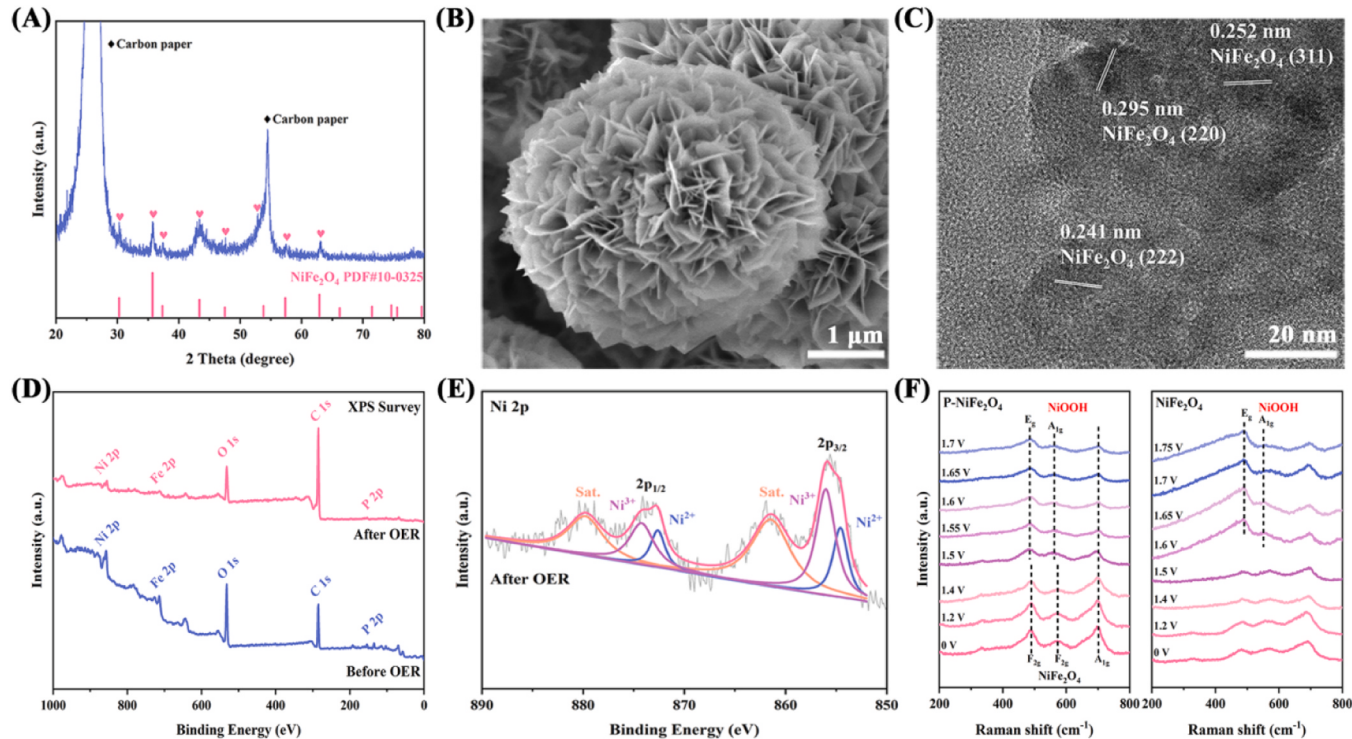


Fig. 4. (A) XRD pattern, (B) SEM image, and (C) HR-TEM image of the post-OER P-NiFe<sub>2</sub>O<sub>4</sub>. (D) The XPS survey profiles of P-NiFe<sub>2</sub>O<sub>4</sub> before and after OER process. (E) High-resolution Ni 2p spectrum of the post-OER P-NiFe<sub>2</sub>O<sub>4</sub>. (F) *In-situ* electrochemical Raman spectra of NiFe<sub>2</sub>O<sub>4</sub> and P-NiFe<sub>2</sub>O<sub>4</sub> in 1.0 M KOH.

high-resolution Fe 2p spectra (Fig. S17), compared with the pristine sample, the ratio of  $\text{Fe}^{3+}/\text{Fe}^{2+}$  also had an obvious increase and the peak intensity decreased, which might be attributed to the oxidation of Fe and possible dissolution of iron (oxy)hydroxides under the relatively high anodic potential during the OER process [41,55,56]. As for O 1 s spectrum of post-OER P-NiFe<sub>2</sub>O<sub>4</sub> (Fig. S18), the peak attributed to the hydroxyl oxygen (-OH, ~532.4 eV) emerged and the proportion was relatively high, also demonstrating the possible surface reconstruction to metal (oxy)hydroxides [57]. To further prove this hypothesis, the *in-situ* electrochemical Raman measurement was also applied on the as-synthesized NiFe<sub>2</sub>O<sub>4</sub> and P-NiFe<sub>2</sub>O<sub>4</sub> electrocatalysts in 1.0 M KOH electrolyte, respectively (Fig. S19). The electrocatalyst was held under the set potentials for at least 5 min before acquiring each spectrum. From the P-NiFe<sub>2</sub>O<sub>4</sub> spectra displayed in Fig. 4 F, the intensity of modes of F<sub>2g</sub> and A<sub>1g</sub> decreased with the gradual increment of the applied potential. When the working potential reached ~1.5 V (vs. RHE), two new Raman peaks at  $\approx 485 \text{ cm}^{-1}$  and  $\approx 562 \text{ cm}^{-1}$  ascribed to E<sub>g</sub> Ni-O bending vibration mode and A<sub>1g</sub> Ni-O stretching vibration of NiOOH structure emerged [58,59]. Besides, when the potential was above 1.5 V, the position of Raman peaks no longer changed and there were no peaks

related to iron species during this process. In addition, *in-situ* Raman spectra of NiFe<sub>2</sub>O<sub>4</sub> were also recorded under the same measurement conditions for comparison. It could be noticed that NiFe<sub>2</sub>O<sub>4</sub> went through similar surface transformation as P-NiFe<sub>2</sub>O<sub>4</sub>, and the typical peaks assigned to NiOOH did not appear until the working potential reached 1.6 V (vs. RHE), higher than that of P-NiFe<sub>2</sub>O<sub>4</sub>. Therefore, according to preceding analyses, the incorporation of phosphorus could reinforce the surface reconstruction and P-(Ni, Fe)OOH species was formed and played as the main phase for catalysis.

### 3.4. Study the mechanism of oxygen evolution

In order to gain more insights into the reaction mechanism and pathway for the oxygen evolution reaction in this work, a series of electrochemical measurements were subsequently conducted. Unlike from the conventional adsorbate evolution mechanism (AEM) with four concerted proton-electron transfer, non-concerted proton-electron transfer process is proposed for the lattice oxygen-mediated mechanism (LOM) [60]. The pH-dependent property for the anodic current is often related to the lattice oxygen oxidation performance [24]. Therefore, in

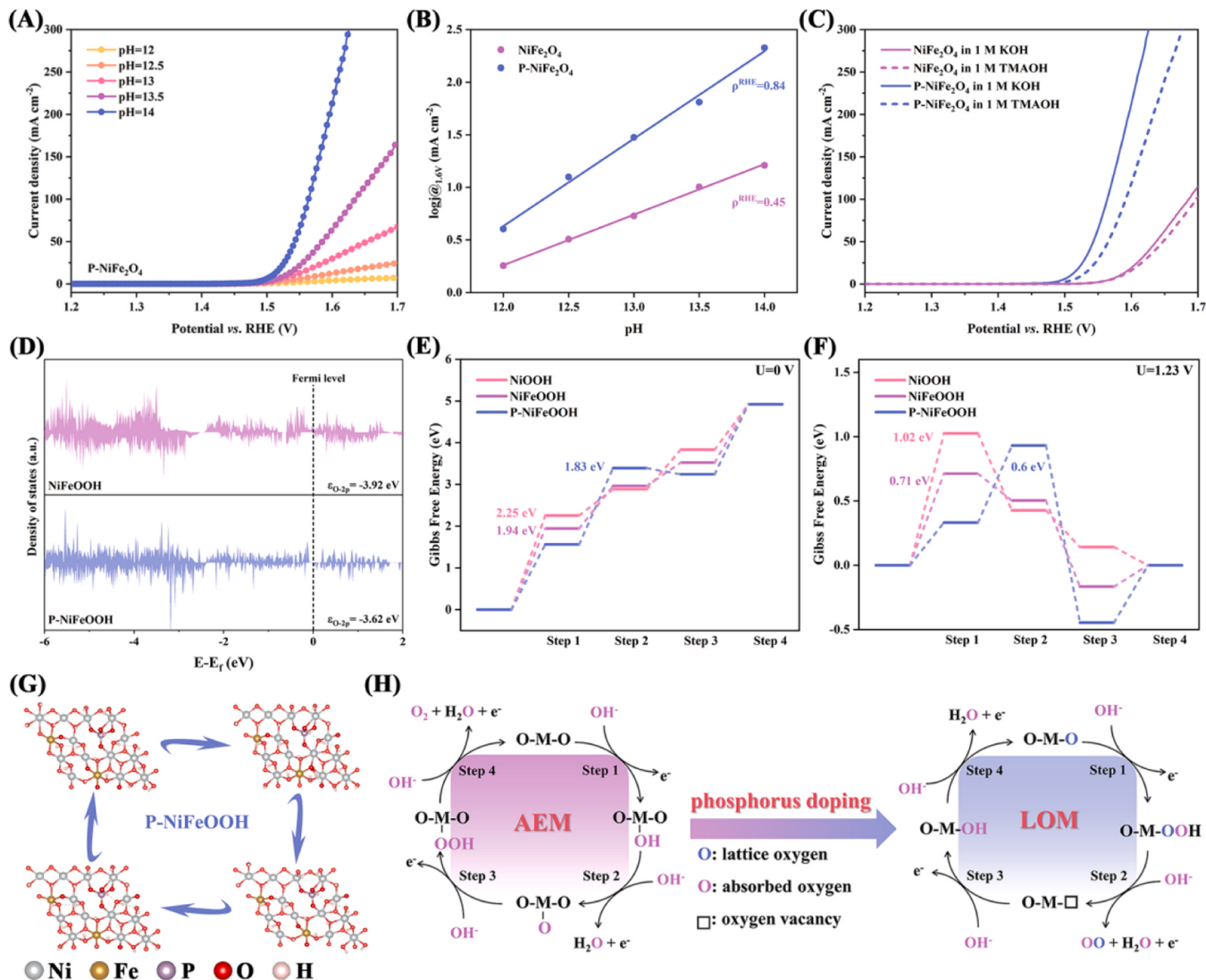


**Fig. 5.** (A) Polarization curves of P-NiFe<sub>2</sub>O<sub>4</sub> in KOH electrolytes with different pH values. (B) The relationship between the logarithm of current density of NiFe<sub>2</sub>O<sub>4</sub> and P-NiFe<sub>2</sub>O<sub>4</sub> at 1.6 V (vs. RHE) and pH. (C) Polarization curves of NiFe<sub>2</sub>O<sub>4</sub> and P-NiFe<sub>2</sub>O<sub>4</sub> in 1.0 M KOH and 1.0 M TMAOH, respectively. (D) Density of states of O 2p of NiFeOOH and P-NiFeOOH. (E) The energetic pathway of OER in the alkaline solution at  $U= 0 \text{ V}$ . (F) The energetic pathway of OER in the alkaline solution at  $U= 1.23 \text{ V}$ . (G) The OER cycles for P-NiFeOOH via LOM route. (H) Proposed adsorbate evolution mechanism (AEM) and lattice oxygen oxidation mechanism (LOM), respectively.

order to investigate the degree of lattice oxygen participation, we first tested the OER performance of  $\text{NiFe}_2\text{O}_4$  and P- $\text{NiFe}_2\text{O}_4$  in KOH electrolytes with different pH values (from 12 to 14). As displayed in Fig. 5 A and Fig. S20, the OER activity of P- $\text{NiFe}_2\text{O}_4$  increased significantly with the rise of pH and exhibited stronger pH dependence than  $\text{NiFe}_2\text{O}_4$ , demonstrating that the non-concerted proton-electron transfer process might occur in P- $\text{NiFe}_2\text{O}_4$  during OER. In addition, we further plotted the histogram of the current densities for  $\text{NiFe}_2\text{O}_4$  and P- $\text{NiFe}_2\text{O}_4$  at 1.6 V (vs. RHE) as a function of pH values (Fig. S21A). In order to demonstrate the correlation between the electrocatalytic activity and the pH values, we also used the proton reaction orders ( $\rho^{\text{RHE}}$ ) on RHE scale [25,26]. As displayed in Fig. 5B, the  $\rho^{\text{RHE}}$  value of P- $\text{NiFe}_2\text{O}_4$  (0.84) was much larger than that of  $\text{NiFe}_2\text{O}_4$  (0.45), suggesting the enhanced lattice oxygen participation even though in a low concentration of hydroxyl ions for P- $\text{NiFe}_2\text{O}_4$ . The results also confirmed that P- $\text{NiFe}_2\text{O}_4$  was dependent on the pH value of the electrolyte and it preferred the LOM pathway for OER.

Based on the phenomenon above, the superperoxo-like ( $\text{O}_2^{\cdot}$ ) and peroxy-like ( $\text{O}_2^{\cdot\cdot}$ ) negative species are always generated in LOM, which could play as a convincing indicator to determine whether LOM dominated the OER route for P- $\text{NiFe}_2\text{O}_4$  [12,61]. The tetramethylammonium cation ( $\text{TMA}^+$ ) could interact with the negative oxygen-containing species strongly, thus hindering the OER performance via LOM route to a large extent [33]. When we changed the electrolyte from KOH to TMAOH, as shown in Fig. 5 C, there was a dramatic decay in the OER activity for P- $\text{NiFe}_2\text{O}_4$  in 1 M TMAOH compared with that in 1 M KOH. On the contrary, negligible reduction in the OER performance and Tafel slope could be observed for pristine  $\text{NiFe}_2\text{O}_4$  (Fig. S21B, C), further demonstrating the enhanced lattice oxygen participation in P- $\text{NiFe}_2\text{O}_4$  to proceed the OER process. Raman spectroscopy was also used to prove the electrostatic interaction between  $\text{TMA}^+$  cation and the negative oxygen-containing species. After P- $\text{NiFe}_2\text{O}_4$  electrode was operated at a constant current density of 10 mA  $\text{cm}^{-2}$  in 1 M TMAOH and washed with deionized water several times, there were new peaks at 456  $\text{cm}^{-1}$  and 752  $\text{cm}^{-1}$  appearing, which were the characteristic peaks of  $\text{TMA}^+$  cation (Fig. S21D) [18,26]. Thus, the analysis results confirmed that the P- $\text{NiFe}_2\text{O}_4$  electrocatalyst preferred the LOM pathway to proceed the OER process, which was also in agreement with the pH-dependent feature discussed above.

On this basis, density functional theory (DFT) calculations were further conducted to probe the intrinsic activity of lattice oxygen. Based on the XPS and *in-situ* Raman results, the reconstructed metal (oxy)hydroxides on the surface of spinel electrocatalysts were selected as the research models. According to the P 2p spectrum of post-OER P- $\text{NiFe}_2\text{O}_4$  (Fig. S22) and some previously reported references, phosphorus species would convert to phosphate during the anodic OER process [52,62,63]. Therefore, in this work, P existed as  $\text{PO}_x$  species in P- $\text{NiFeOOH}$  model rather than simple doping or replacement, and the optimized computational models were displayed in Fig. S23. The distance between the O 2p band center and Fermi level ( $E_F$ ) has been considered as an important descriptor to identify the activity of lattice oxygen [26]. Hence, the projected density of states (PDOS) of O 2p orbitals of  $\text{NiFeOOH}$  and P- $\text{NiFeOOH}$  were calculated. As shown in Fig. 5D, after the introduction of phosphorus, the O 2p band center ( $\epsilon_{\text{O-}2\text{p}}$ ) energy had an obvious upshift from  $-3.92$  eV for  $\text{NiFeOOH}$  to  $-3.62$  eV for P- $\text{NiFeOOH}$ . The closer the *p*-band center is to  $E_F$ , the more easily the lattice oxygen releases from the lattice and promotes the LOM mechanism. The uplifted O 2p could promote the oxygen redox reaction under anodic potential and the lattice oxygen atoms would be more active to participate into the formation of oxygen molecules [4,64].

Furthermore, the total density of states (DOS) of P- $\text{NiFeOOH}$  was continuous near the  $E_F$ , proving its superior electrical conductivity (Fig. S24). Subsequently, based on the LOM pathway, the Gibbs adsorption energies of the oxygen reaction intermediates ( ${}^*\text{O}$ ,  ${}^*\text{OOH}$ ,  ${}^*\text{OO}$ ,  $\text{V}_0$ ) produced in the elementary steps were also calculated for  $\text{NiOOH}$ ,  $\text{NiFeOOH}$  and P- $\text{NiFeOOH}$ , respectively (Fig. 5E-G, Fig. S25).

The results demonstrated that both  $\text{NiOOH}$  and  $\text{NiFeOOH}$  required relatively higher overpotentials to drive the reaction via LOM route, with energy barriers of 2.25 eV and 1.94 eV. For comparison, the rate-determining step (RDS) for P- $\text{NiFeOOH}$  reduced to 1.83 eV theoretically to realize the whole process. According to preceding results, the reconstructed P- $\text{NiFeOOH}$  composite was much easier to proceed OER through LOM pathway, and the introduction of phosphorus into spinel  $\text{NiFe}_2\text{O}_4$  could help to balance and optimize the intermediate adsorption energy on the surface of the electrocatalyst, thus boosting the water oxidation performance as a result (Fig. 5H). To summarize, the incorporated phosphorus could enhance the TM-O hybridization and reduce the energy barrier to proceed OER process.

#### 4. Conclusion

In summary, we have successfully synthesized 2D spinel  $\text{NiFe}_2\text{O}_4$  nanosheets and introduced phosphorus into them by the simple *in-situ* phosphating method. It is shown that the prepared P- $\text{NiFe}_2\text{O}_4$  catalyst showed much more improved and desirable electrocatalytic performance than  $\text{NiFe}_2\text{O}_4$  towards OER process with an overpotential of 264 mV at 10 mA  $\text{cm}^{-2}$  in alkaline solution, which was contributed to the increased active surface area, improved electronic conductivity and optimized electronic structure. Experimental results have suggested the strong pH-dependent property of P- $\text{NiFe}_2\text{O}_4$  electrocatalyst and confirmed the enhancement of lattice oxygen participation and the dominant role of LOM mechanism after the incorporation of phosphorus into  $\text{NiFe}_2\text{O}_4$ . Theoretical calculations were carried out to investigate the reason for the improvement of the electrocatalytic performance. The calculation results revealed that the incorporated phosphorus could not only upshift the position of O 2p band relative to Fermi level ( $E_F$ ) but also could regulate the adsorption behavior of the oxygen-containing intermediates, thus benefiting LOM and realizing high electrocatalytic activity. We hope that this work could offer some guidelines for the design and development of spinel-based OER electrocatalysts with high efficiency and performance towards water splitting.

#### CRediT authorship contribution statement

**Shouhua Feng:** Software, Resources. **Haiyan Lu:** Supervision. **Zhan Shi:** Writing – review & editing, Supervision, Resources, Funding acquisition. **Yuxin Li:** Writing – original draft, Methodology, Investigation, Formal analysis. **Zhe Zhang:** Methodology, Formal analysis. **Xiao-Bo Chen:** Writing – review & editing. **Chunguang Li:** Supervision. **Yong Zhou:** Methodology, Investigation.

#### Declaration of Competing Interest

The authors declare that they have no known competing financial interests or personal relationships that could have appeared to influence the work reported in this paper.

#### Data availability

Data will be made available on request.

#### Acknowledgments

This work was financially supported by the National Natural Science Foundation of China (22271114) and 111 Project (B17020). The authors also gratefully acknowledge the financial support by the program for JLU Science and Technology Innovative Research Team (JLUSTIRT).

#### Appendix A. Supporting information

Supplementary data associated with this article can be found in the online version at doi:10.1016/j.apcatb.2024.124116.

## References

- [1] Z. Liu, Z. Kong, S. Cui, L. Liu, F. Wang, Y. Wang, S. Wang, S. Quan Zang, Electrocatalytic mechanism of defect in spinels for water and organics oxidation, *Small* 19 (2023) 2302216.
- [2] Y. Duan, J.Y. Lee, S. Xi, Y. Sun, J. Ge, S.J.H. Ong, Y. Chen, S. Dou, F. Meng, C. Diao, A.C. Fisher, X. Wang, G.G. Scherer, A. Grimaud, Z.J. Xu, Anodic oxidation enabled cation leaching for promoting surface reconstruction in water oxidation, *Angew. Chem.* 133 (2021) 7494–7501.
- [3] C. Zhao, J. Wang, Y. Gao, J. Zhang, C. Huang, Q. Shi, S. Mu, Q. Xiao, S. Huo, Z. Xia, J. Zhang, X. Lu, Y. Zhao, D-orbital manipulated ru nanoclusters for high-efficiency overall water splitting at industrial-level current densities, *Adv. Funct. Mater.* 34 (2023) 2307917.
- [4] Y. Sun, J. Wu, Y. Xie, X. Wang, K. Ma, Z. Tian, Z. Zhang, Q. Liao, W. Zheng, Z. Kang, Y. Zhang, Dynamics of both active phase and catalysis pathway for spinel water-oxidation catalysts, *Adv. Funct. Mater.* 32 (2022) 2207116.
- [5] J. Sun, H. Xue, Y.F. Zhang, X.L. Zhang, N. Guo, T. Song, H. Dong, Y. Kong, J. Zhang, Q. Wang, Unraveling the synergistic effect of heteroatomic substitution and vacancy engineering in  $\text{CoFe}_2\text{O}_4$  for superior electrocatalysis performance, *Nano Lett.* 22 (2022) 3503–3511.
- [6] J. Sun, H. Xue, N. Guo, T. Song, Y. ru Hao, J. Sun, J. Zhang, Q. Wang, Synergetic metal defect and surface chemical reconstruction into  $\text{NiCo}_2\text{S}_4/\text{ZnS}$  heterojunction to achieve outstanding oxygen evolution performance, *Angew. Chem. - Int. Ed.* 60 (2021) 19435–19441.
- [7] J. Song, C. Wei, Z.F. Huang, C. Liu, L. Zeng, X. Wang, Z.J. Xu, A review on fundamentals for designing oxygen evolution electrocatalysts, *Chem. Soc. Rev.* 49 (2020) 2196–2214.
- [8] T. Liu, M. Guo, A. Orthaber, R. Lomoth, M. Lundberg, S. Ott, L. Hammarström, Accelerating proton-coupled electron transfer of metal hydrides in catalyst model reactions, *Nat. Chem.* 10 (2018) 881–887.
- [9] C. Hu, L. Zhang, J. Gong, Recent progress made in the mechanism comprehension and design of electrocatalysts for alkaline water splitting, *Energy Environ. Sci.* 12 (2019) 2620–2645.
- [10] Z.F. Huang, J. Song, Y. Du, S. Xi, S. Dou, J.M.V. Nsanzimana, C. Wang, Z.J. Xu, X. Wang, Chemical and structural origin of lattice oxygen oxidation in Co-Zn oxyhydroxide oxygen evolution electrocatalysts, *Nat. Energy* 4 (2019) 329–338.
- [11] L. Tang, Y. Yang, H. Guo, Y. Wang, M. Wang, Z. Liu, G. Yang, X. Fu, Y. Luo, C. Jiang, Y. Zhao, Z. Shao, Y. Sun, High configuration entropy activated lattice oxygen for O<sub>2</sub> formation on perovskite electrocatalyst, *Adv. Funct. Mater.* 32 (2022) 2112157.
- [12] X. Li, C. Deng, Y. Kong, Q. Huo, L. Mi, J. Sun, J. Cao, J. Shao, X. Chen, W. Zhou, M. Lv, X. Chai, H. Yang, Q. Hu, C. He, Unlocking the transition of electrochemical water oxidation mechanism induced by heteroatom doping, *Angew. Chem. Int. Ed.* 62 (2023) 2309732.
- [13] J.S. Yoo, X. Rong, Y. Liu, A.M. Kolpak, Role of lattice oxygen participation in understanding trends in the oxygen evolution reaction on perovskites, *ACS Catal.* 8 (2018) 4628–4636.
- [14] S. Xin, Y. Tang, B. Jia, Z. Zhang, C. Li, R. Bao, C. Li, J. Yi, J. Wang, T. Ma, Coupling adsorbed evolution and lattice oxygen mechanism in  $\text{Fe-Co(OH)}_2/\text{Fe}_2\text{O}_3$  heterostructure for enhanced electrochemical water oxidation, *Adv. Funct. Mater.* 33 (2023) 2305243.
- [15] Y. Duan, S. Sun, Y. Sun, S. Xi, X. Chi, Q. Zhang, X. Ren, J. Wang, S.J.H. Ong, Y. Du, L. Gu, A. Grimaud, Z.J. Xu, Mastering surface reconstruction of metastable spinel oxides for better water oxidation, *Adv. Mater.* 31 (2019) 1807898.
- [16] W. Hooch Antink, S. Lee, H.S. Lee, H. Shin, T.Y. Yoo, W. Ko, J. Shim, G. Na, Y. E. Sung, T. Hyeon, High-valence metal-driven electronic modulation for boosting oxygen evolution reaction in high-entropy spinel oxide, *Adv. Funct. Mater.* 34 (2023) 2309438.
- [17] E. Fabbri, T.J. Schmidt, Oxygen evolution reaction - the enigma in water electrolysis, *ACS Catal.* 8 (2018) 9765–9774.
- [18] Z.F. Huang, S. Xi, J. Song, S. Dou, X. Li, Y. Du, C. Diao, Z.J. Xu, X. Wang, Tuning of lattice oxygen reactivity and scaling relation to construct better oxygen evolution electrocatalyst, *Nat. Commun.* 12 (2021) 3992.
- [19] J. Zhang, J. Qian, J. Ran, P. Xi, L. Yang, D. Gao, Engineering lower coordination atoms onto  $\text{NiO/Co}_3\text{O}_4$  heterointerfaces for boosting oxygen evolution reactions, *ACS Catal.* 10 (2020) 12376–12384.
- [20] S. Sun, X. Zhou, B. Cong, W. Hong, G. Chen, Tailoring the d-band centers endows  $(\text{Ni}_{x}\text{Fe}_{1-x})_2\text{P}$  nanosheets with efficient oxygen evolution catalysis, *ACS Catal.* 10 (2020) 9086–9097.
- [21] Z. Wang, J. Huang, L. Wang, Y. Liu, W. Liu, S. Zhao, Z.Q. Liu, Cation-tuning induced d-band center modulation on co-based spinel oxide for oxygen reduction/evolution reaction, *Angew. Chem. - Int. Ed.* 61 (2022) 2114696.
- [22] H. Wang, T. Zhai, Y. Wu, T. Zhou, B. Zhou, C. Shang, Z. Guo, High-valence oxides for high performance oxygen evolution electrocatalysis, *Adv. Sci.* 10 (2023) 2301706.
- [23] Y. Pan, X. Xu, Y. Zhong, L. Ge, Y. Chen, J.P.M. Veder, D. Guan, R. O'Hayre, M. Li, G. Wang, H. Wang, W. Zhou, Z. Shao, Direct evidence of boosted oxygen evolution over perovskite by enhanced lattice oxygen participation, *Nat. Commun.* 11 (2020) 2002.
- [24] W. Zhai, Y. Chen, Y. Liu, T. Sakthivel, Y. Ma, Y. Qin, Y. Qu, Z. Dai, Enlarging the Ni-O bond polarizability in a phosphorene-hosted metal-organic framework for boosted water oxidation electrocatalysis, *ACS Nano* 17 (2023) 17254–17264.
- [25] R. Chen, Z. Wang, S. Chen, W. Wu, Y. Zhu, J. Zhong, N. Cheng, Activating lattice oxygen in spinel oxides via engineering octahedral sites for oxygen evolution, *ACS Energy Lett.* 8 (2023) 3504–3511.
- [26] F. Wang, P. Zou, Y. Zhang, W. Pan, Y. Li, L. Liang, C. Chen, H. Liu, S. Zheng, Activating lattice oxygen in high-entropy LDH for robust and durable water oxidation, *Nat. Commun.* 14 (2023) 6019.
- [27] L. Huang, D. Chen, G. Luo, Y.R. Lu, C. Chen, Y. Zou, C.L. Dong, Y. Li, S. Wang, Zirconium-regulation-induced bifunctionality in 3D cobalt–iron oxide nanosheets for overall water splitting, *Adv. Mater.* 31 (2019) 1901439.
- [28] Y. Peng, C. Huang, J. Huang, M. Feng, X. Qiu, X. Yue, S. Huang, Filling octahedral interstices by building geometrical defects to construct active sites for boosting the oxygen evolution reaction on  $\text{NiFe}_2\text{O}_4$ , *Adv. Funct. Mater.* 32 (2022) 2201011.
- [29] Y. Zhou, S. Sun, C. Wei, Y. Sun, P. Xi, Z. Feng, Z.J. Xu, Significance of engineering the octahedral units to promote the oxygen evolution reaction of spinel oxides, *Adv. Mater.* 31 (2019) 1902509.
- [30] J.O. Olowoyo, R.J. Kriek, Recent progress on bimetallic-based spinels as electrocatalysts for the oxygen evolution reaction, *Small* 18 (2022) 2203125.
- [31] S. Sun, Y. Sun, Y. Zhou, S. Xi, X. Ren, B. Huang, H. Liao, L.P. Wang, Y. Du, Z.J. Xu, Shifting oxygen charge towards octahedral metal: a way to promote water oxidation on cobalt spinel oxides, *Angew. Chem. - Int. Ed.* 58 (2019) 6042–6047.
- [32] J. Sun, N. Guo, Z. Shao, K. Huang, Y. Li, F. He, Q. Wang, A Facile strategy to construct amorphous spinel-based electrocatalysts with massive oxygen vacancies using ionic liquid dopant, *Adv. Energy Mater.* 8 (2018) 1800980.
- [33] X. Chen, Q. Wang, Y. Cheng, H. Xing, J. Li, X. Zhu, L. Ma, Y. Li, D. Liu, S-doping triggers redox reactivities of both iron and lattice oxygen in feooh for low-cost and high-performance water oxidation, *Adv. Funct. Mater.* 32 (2022) 2112674.
- [34] H. Liang, A.N. Gandi, D.H. Anjum, X. Wang, U. Schwingenschlo, H.N. Alshraef, 2016, , *Plasma-Assisted Synthesis of NiCoP for Efficient Overall Water Splitting* 167718–7725.
- [35] R. Zhang, Z. Wei, G. Ye, G. Chen, J. Miao, X. Zhou, X. Zhu, X. Cao, X. Sun, “d-electron complementation” induced V-Co phosphide for efficient overall water splitting, *Adv. Energy Mater.* 11 (2021) 2101758.
- [36] Y. Song, M. Sun, S. Zhang, X. Zhang, P. Yi, J. Liu, B. Huang, M. Huang, L. Zhang, Alleviating the work function of vein-like  $\text{Co}_3\text{P}$  by Cr doping for enhanced seawater electrolysis, *Adv. Funct. Mater.* 33 (2023) 2214081.
- [37] H.J. Liu, R.N. Luan, L.Y. Li, R.Q. Lv, Y.M. Chai, B. Dong, Sulphur-dopant induced breaking of the scaling relation on low-valence Ni sites in nickel ferrite nanocoines for water oxidation with industrial-level current density, *Chem. Eng. J.* 461 (2023) 141714.
- [38] J. Jin, J. Yin, H. Liu, B. Huang, Y. Hu, H. Zhang, M. Sun, Y. Peng, P. Xi, C.H. Yan, Atomic sulfur filling oxygen vacancies optimizes H absorption and boosts the hydrogen evolution reaction in alkaline media, *Angew. Chem. - Int. Ed.* 60 (2021) 14117–14123.
- [39] C. Ouyang, X. Wang, S. Wang, Phosphorus-doped  $\text{Co}_2$  nanosheet arrays as ultra-efficient electrocatalysts for the hydrogen evolution reaction, *Chem. Commun.* 51 (2015) 14160–14163.
- [40] Y. Qi, X. Xiao, Y. Mei, L. Xiong, L. Chen, X. Lin, Z. Lin, S. Sun, B. Han, D. Yang, Y. Qin, X. Qiu, Modulation of Brønsted and Lewis acid centers for  $\text{Ni}_x\text{Co}_{3-x}\text{O}_4$  spinel catalysts: towards efficient catalytic conversion of lignin, *Adv. Funct. Mater.* 32 (2022) 2111615.
- [41] S. Hong, K. Ham, J. Hwang, S. Kang, M.H. Seo, Y.W. Choi, B. Han, J. Lee, K. Cho, Active motif change of Ni-Fe spinel oxide by Ir doping for highly durable and facile oxygen evolution reaction, *Adv. Funct. Mater.* 33 (2023) 2209543.
- [42] Z. Xiao, Y. Wang, Y.C. Huang, Z. Wei, C.L. Dong, J. Ma, S. Shen, Y. Li, S. Wang, Filling the oxygen vacancies in  $\text{Co}_3\text{O}_4$  with phosphorus: an ultra-efficient electrocatalyst for overall water splitting, *Energy Environ. Sci.* 10 (2017) 2563–2569.
- [43] X. Yue, X. Qin, Y. Chen, Y. Peng, C. Liang, M. Feng, X. Qiu, M. Shao, S. Huang, Constructing active sites from atomic-scale geometrical engineering in spinel oxide solid solutions for efficient and robust oxygen evolution reaction electrocatalysts, *Adv. Sci.* 8 (2021) 2101653.
- [44] Y. Li, Z. Zhang, Z. Zhang, J. He, M. Xie, C. Li, H. Lu, Z. Shi, S. Feng, Construction of  $\text{Ni}_2\text{P}-\text{NiFe}_2\text{O}_4$  heterostructured nanosheets towards performance-enhanced water oxidation reaction, *Appl. Catal. B Environ.* 339 (2023) 123141.
- [45] J. Zheng, X. Peng, Z. Xu, J. Gong, Z. Wang, Cationic defect engineering in spinel  $\text{NiCo}_2\text{O}_4$  for enhanced electrocatalytic oxygen evolution, *ACS Catal.* 12 (2022) 10245–10254.
- [46] Y. Wu, J. Yang, T. Tu, W. Li, P. Zhang, Y. Zhou, J. Li, J. Li, S. Sun, Evolution of cationic vacancy defects: a motif for surface restructuring of OER precatalyst, *Angew. Chem.* 133 (2021) 27033–27040.
- [47] C.F. Li, J.W. Zhao, L.J. Xie, J.Q. Wu, G.R. Li, Fe doping and oxygen vacancy modulated Fe-Ni<sub>5</sub>P<sub>4</sub>/NiFeOH nanosheets as bifunctional electrocatalysts for efficient overall water splitting, *Appl. Catal. B Environ.* 291 (2021) 119987.
- [48] W. Yang, Y. Bai, L. Peng, M. Qu, K. Sun, Enhanced oxygen evolution performance of iron-nickel oxide catalyst through dual-defect engineering, *J. Colloid Interface Sci.* 648 (2023) 701–708.
- [49] T. Zhang, K. Yang, C. Wang, S. Li, Q. Zhang, X. Chang, J. Li, S. Li, S. Jia, J. Wang, L. Fu, Nanometric Ni<sub>5</sub>P<sub>4</sub> clusters nested on  $\text{NiCo}_2\text{O}_4$  for efficient hydrogen production via alkaline water electrolysis, *Adv. Energy Mater.* 8 (2018) 1801690.
- [50] L. Ji, J. Wang, X. Teng, T.J. Meyer, Z. Chen, CoP nanoframes as bifunctional electrocatalysts for efficient overall water splitting, *ACS Catal.* 10 (2020) 412–419.
- [51] Y. Yan, J. Lin, K. Huang, X. Zheng, L. Qiao, S. Liu, J. Cao, S.C. Jun, Y. Yamauchi, J. Qi, Tensile strain-mediated spinel ferrites enable superior oxygen evolution activity, *J. Am. Chem. Soc.* 145 (2023) 24218–24229.
- [52] T. Zhang, Y. Liu, L. Tong, J. Yu, S. Lin, Y. Li, H.J. Fan, Oxidation state engineering in octahedral Ni by anchored sulfide to boost intrinsic oxygen evolution activity, *ACS Nano* 17 (2023) 6770–6780.
- [53] X. Du, M. Tan, T. Wei, H. Kobayashi, J. Song, Z. Peng, H. Zhu, Z. Jin, R. Li, W. Liu, Highly efficient and robust nickel-iron bifunctional catalyst coupling selective

methanol oxidation and freshwater/seawater hydrogen evolution via CO-free pathway, *Chem. Eng. J.* 452 (2023) 139404.

[54] M. Wang, S. Ji, H. Wang, X. Wang, V. Linkov, R. Wang, Foamed carbon-Supported nickel-iron oxides interspersed with bamboo-like carbon nanotubes for high-performance rechargeable zinc-air batteries, *Small* 18 (2022) 2204474.

[55] D.Y. Chung, P.P. Lopes, P. Farinazzo Bergamo Dias Martins, H. He, T. Kawaguchi, P. Zapol, H. You, D. Tripkovic, D. Strmcnik, Y. Zhu, S. Seifert, S. Lee, V. R. Stamenkovic, N.M. Markovic, Dynamic stability of active sites in hydr(oxy) oxides for the oxygen evolution reaction, *Nat. Energy* 5 (2020) 222–230.

[56] Q. Han, Y. Luo, J. Li, X. Du, S. Sun, Y. Wang, G. Liu, Z. Chen, Efficient NiFe-based oxygen evolution electrocatalysts and origin of their distinct activity, *Appl. Catal. B Environ.* 304 (2022) 120937.

[57] J. Yin, Y. Li, F. Lv, M. Lu, K. Sun, W. Wang, L. Wang, F. Cheng, Y. Li, P. Xi, S. Guo, Oxygen vacancies dominated  $\text{NiS}_2/\text{CoS}_2$  interface porous nanowires for portable Zn-air batteries driven water splitting devices, *Adv. Mater.* 29 (2017) 1704681.

[58] J. Li, Y. Liu, H. Chen, Z. Zhang, X. Zou, Design of a multilayered oxygen-evolution electrode with high catalytic activity and corrosion resistance for saline water splitting, *Adv. Funct. Mater.* 31 (2021) 2101820.

[59] N. Zhang, Y. Hu, L. An, Q. Li, J. Yin, J. Li, R. Yang, M. Lu, S. Zhang, P. Xi, C.H. Yan, Surface activation and Ni-S stabilization in  $\text{NiO}/\text{NiS}_2$  for efficient oxygen evolution reaction, *Angew. Chem. - Int. Ed.* 61 (2022) 2207217.

[60] K. Xiao, Y. Wang, P. Wu, L. Hou, Z.Q. Liu, Activating lattice oxygen in spinel  $\text{ZnCo}_2\text{O}_4$  through filling oxygen vacancies with fluorine for electrocatalytic oxygen evolution, *Angew. Chem. - Int. Ed.* 62 (2023) 2301408.

[61] H. Liu, X. Li, C. Peng, L. Zhu, Y. Zhang, H. Cheng, J. Cui, Q. Wu, Y. Zhang, Z. Chen, W. Zou, W. Gu, H. Huang, J. Wang, B. Ye, Z. Fu, Y. Lu, Activating the lattice oxygen in  $(\text{Bi}_{0.5}\text{Co}_{0.5})_2\text{O}_3$  by vacancy modulation for efficient electrochemical water oxidation, *J. Mater. Chem. A* 8 (2020) 13150–13159.

[62] Y. Shi, W. Du, W. Zhou, C. Wang, S. Lu, S. Lu, B. Zhang, Unveiling the promotion of surface-adsorbed chalcogenate on the electrocatalytic oxygen evolution reaction, *Angew. Chem. - Int. Ed.* 59 (2020) 22470–22474.

[63] S. Li, R. Ma, J. Hu, Z. Li, L. Liu, X. Wang, Y. Lu, G.E. Sterbinsky, S. Liu, L. Zheng, J. Liu, D. Liu, J. Wang, Coordination environment tuning of nickel sites by oxyanions to optimize methanol electro-oxidation activity, *Nat. Commun.* 13 (2022) 2916.

[64] Z. He, J. Zhang, Z. Gong, H. Lei, D. Zhou, N. Zhang, W. Mai, S. Zhao, Y. Chen, Activating lattice oxygen in NiFe-based (oxy)hydroxide for water electrolysis, *Nat. Commun.* 13 (2022) 2191.